A Combined SAR Doppler Centroid Estimation Scheme Based upon Signal Phase

Frank Wong, *Member, IEEE,* and Ian G. Cumming, *Member, IEEE*

***Abstract*—This paper describes a complete end-to-end Doppler centroid estimation scheme, which determines the fractional PRF part of the Doppler centroid. It also resolves the Doppler ambiguity. Experiments show that the scheme works successfully over various terrain types, including land, water, and ice, and that it requires only a modest amount of SAR data to perform reliably. The proposed scheme has an added advantage that it is directly applicable to RADARSAT and ENVISAT ScanSAR data.**

The scheme uses two complementary Doppler estimation algorithms, both utilizing the phase information embedded in the radar signal. In each algorithm, upper and lower parts of the available bandwidth of the received signal are extracted to form two range looks. The first algorithm, called multilook cross correlation (MLCC), computes the average cross correlation coefficient between adjacent azimuth samples for each of the two looks and then takes the difference between the angles of the two coefficients. The Doppler ambiguity is determined from the angle difference. The fractional pulse repetition frequency (PRF) part is also determined from the cross correlation coefficients. In the second algorithm, called multilook beat frequency (MLBF), the two looks are multiplied together to generate a beat signal. The beat frequency is then estimated and the Doppler ambiguity determined from the beat frequency.

The MLCC algorithm performs better with low contrast scenes while the MLBF works better with high contrast ones. Although each algorithm works well on its own with sufficient averaging, it is also possible to use quality measures to select the best result from either algorithm. In this way, scenes of different content or contrast can be handled reliably. This paper presents the analysis of the two algorithms, explaining why their performance is affected by scene contrast, which is confirmed by experimental results with ERS-1 and JERS-1 data.

I. Introduction

DOPPLER centroid estimators are needed in SAR processing to establish parameters required for operations such as range cell migration correction, azimuth compression, and image registration. In general, the Doppler centroid has to be accurate to within 5–10% of the azimuth bandwidth to meet image quality specifications for signal to noise ratio and signal to ambiguity ratio. In some SAR systems, antenna pointing information is sufficient to compute the required parameters, but for many systems, such as satellite SAR's, a more accurate Doppler centroid must be estimated from the received data [1].

Manuscript received March 2, 1995; revised October 5, 1995. This work was supported by MacDonald Dettwiler, the Natural Sciences and Engineering Research Council, the BC Advanced Systems Institute (ASI), and the BC Science Council.

F. Wong was with the Department of Electrical Engineering, University of British Columbia, Vancouver V6T 1Z4 Canada, on leave from MacDonald Dettwiler and Associates, Richmond, B.C. V6V 2J3 Canada.

I. G. Cumming is with the Department of Electrical Engineering, University of British Columbia, Vancouver V6T 1Z4 Canada.

Publisher Item Identifier S 0196-2892(96)02845-8.

As the Doppler centroid is aliased by the sampling of the pulse repetition frequency (PRF), it can be considered to be made up of an "integer PRF part" and a "fractional PRF part." The fractional PRF part is the centroid wrapped around to the fundamental frequency range of the PRF, and the integer PRF part is referred to as the *Doppler ambiguity.* The shape of the Doppler spectrum due to the azimuth beam pattern is readily apparent in the aliased received data, and a number of methods can be used to estimate the fractional part. However, because of the aliasing, a more complicated approach must be used to estimate the Doppler ambiguity, which is not readily apparent in the received data.

In this paper, we present an integrated Doppler estimator which estimates both the integer and fractional parts of the Doppler centroid from the SAR data. The estimator determines the *absolute* Doppler frequency, without aliasing, and so obtains both of the parameters as a function of range. Knowledge of the beam pointing angles is not needed by the algorithm, except as a crosscheck.

A traditional approach to estimating the fractional PRF part is to use a correlation and regression procedure to locate the centroid of the aliased Doppler spectrum in a sample of the image [2]. This method has proven to be reliable for satellite SAR data, but sometimes requires filtering in areas of high contrast. In addition, it requires taking the azimuth fast Fourier transform (FFT) of large blocks of data, which is not convenient for ScanSAR data [3].

In order to improve the estimator accuracy, various authors have sought ways to utilize signal phase in the estimation algorithm. In 1989, Madsen [4] used an algorithm based on estimating phase increments in raw signal data; the method was originally applied to spectral estimation in other fields [5], [6]. The phase increments are estimated by taking the average cross correlation coefficient (ACCC) between adjacent azimuth samples (the average of the product of one sample times the complex conjugate of the next sample). This method fits in naturally with the present method, as little extra computation is needed, and gives a more accurate fractional estimate than the methods which obtain the absolute Doppler centroid.

A commonly-used Doppler ambiguity resolver (DAR) is based on the property that the range cell migration is a function of the ambiguity. The method uses an azimuth look correlation technique [7], in which the correlation is performed in the range direction on detected image amplitude. The method works well for many scenes, but lacks sensitivity as the correlation lag is in the order of only one or two cells per ambiguity for C-band satellites. This lack of sensitivity means

that the method is not always reliable in areas of low scene contrast.

In 1991, the German Aerospace Establishment (DLR) developed a Doppler centroid estimator [8] based upon the property that the absolute Doppler centroid is a function of the frequency of the transmitted signal. The algorithm works in the range frequency domain, in which the various frequencies in the transmitted signal can be identified. It computes the ACCC between adjacent azimuth samples at each range frequency cell, then estimates the slope and intercept of the ACCC angle as a function of range frequency. The absolute Doppler centroid frequency can be obtained from the slope, from which the Doppler ambiguity is obtained. The slope is not accurate enough to estimate the fractional part, but the intercept can be used to obtain the fractional part more accurately.

In practice, different scene areas tend to have different contrast which would affect the performance of any estimator. The DLR algorithm works best in areas of low contrast such as ice or water. The algorithm still works for high contrast areas, as long as more data is averaged when obtaining the ACCC angle.

A distinction of the newer algorithms is that they use signal *phase* rather than amplitude as the primary measurement in the estimation process. This gives the measurements more sensitivity. In this paper, we will build upon previous concepts to develop an integrated estimator based on signal phase. Two new algorithms have been developed which also use the property that the absolute Doppler centroid is a function of the frequency of the transmitted signal.

One algorithm, called the multilook beat frequency (MLBF) algorithm, is based on multiplying two range looks together, and using an FFT to estimate the resultant beat frequency. The beat frequency arises from the beating of the response of a scatterer at two different transmitted frequencies, and is a function of the absolute Doppler centroid. The Doppler ambiguity can be effectively estimated in this way, especially for high contrast scenes. However, the estimate is not accurate enough to effectively estimate the fractional PRF part. The MLBF algorithm will be described in Section II-C.

While developing the MLBF algorithm, it was recognized that the ACCC angle of the two looks can be computed, and that the difference between the two ACCC angles can be used to compute the absolute Doppler centroid. A second algorithm was developed based on this principle, and will be called the multilook cross correlation (MLCC) method. This method is different from the MLBF algorithm in that it works best for low contrast scenes, as does the DLR method. It shares some common features with the DLR method, but differs from the DLR method in that it works in the range time domain rather than the range frequency domain. This has the advantage of keeping the range dependence of the azimuth FM rate (and hence the range dependence of the Doppler centroid) clearly distinct. The MLCC algorithm will be described in Section II-B.

Since the MLBF and MLCC methods have complementary properties, and the most time-consuming computational step of multilook range compression is common to both methods, it was decided to develop a Doppler centroid estimation scheme which combined both algorithms. The word "scheme" is used to refer to the entire estimation process to distinguish it from the two constituent algorithms. In this way, a robust Doppler estimator can be built which works well in all types of SAR scenes with an adequate signal to noise ratio.

In this paper, the MLBF and MLCC algorithms will be described, as well as how they are combined into one scheme. Section II describes and analyzes the two algorithms, illustrating their operation using a point target. The performance of either algorithm is affected by the presence of multiple targets in the scene because their phases interfere with each other. This interference between multiple targets is studied in Section III. It turns out that the multitarget interference improves the performance of the MLCC algorithm, but degrades the MLBF algorithm, which explains why the former works best in low contrast scenes, while the latter works best with high contrast scenes.

Experiments with ERS-1 and JERS-1 data were performed, and the results show that the scheme works successfully over a variety of terrain types, including land, sea and ice. The scheme requires only a 4-K × 4-K (K = 1024) block of data to work reliably, but additional averaging does improve the estimate. This is equal to or less than the volume of data required by other Doppler estimators. Section IV presents the experimental results, and Section V summarizes the properties of the new scheme.

II. Algorithm Description

This section describes the MLCC and MLBF Doppler ambiguity resolving algorithms, and then the overall Doppler estimation scheme.

A. Phase Properties of Range Look Data

The operation of the algorithms is illustrated by considering two range compressed looks of a single point target. Ignoring the target's complex amplitude and range envelope, the range compressed signals of the two looks $S_1(\eta)$ and $S_2(\eta)$ are given by

$$S_1(\eta) = W(\eta - \eta_c) \exp\left[\frac{-j4\pi\left(f_0 - \frac{\Delta f}{2}\right)R(\eta)}{c}\right] \quad (1)$$

$$S_2(\eta) = W(\eta - \eta_c) \exp\left[\frac{-j4\pi\left(f_0 + \frac{\Delta f}{2}\right)R(\eta)}{c}\right] \quad (2)$$

where $j^2 = -1$, η = azimuth time from zero Doppler, η_c = Doppler centroid time, $W(\eta)$ = azimuth envelope, f_0 = center transmitted frequency, Δf = frequency separation between the two range looks, $R(\eta)$ = instantaneous slant range, and c = speed of light.

The phase arguments in (1) and (2) give the azimuth phase history of the target, which are different between looks 1 and 2 because of the frequency shift Δf.

The instantaneous slant range $R(\eta)$ can be written as

$$R(\eta) = \sqrt{R_0^2 + B\eta^2} \approx R_0 + \frac{B}{2R_0}\eta^2 \tag{3}$$

where R_0 is the slant range of closest approach, and B is the square of the effective velocity between the radar and the target. Ignoring constant phase terms, (1) and (2) can then be written in the following familiar forms:

$$S_1(\eta) = W(\eta - \eta_c)\exp(-j\pi K_{a_1}\eta^2) \tag{4}$$

$$S_2(\eta) = W(\eta - \eta_c)\exp(-j\pi K_{a_2}\eta^2) \tag{5}$$

where K_{a1} and K_{a_2} are the azimuth FM rate of the two looks given respectively by

$$K_{a_1} = \frac{2B\left(f_0 - \frac{\Delta f}{2}\right)}{cR_0} \tag{6}$$

$$K_{a_2} = \frac{2B\left(f_0 + \frac{\Delta f}{2}\right)}{cR_0}. \tag{7}$$

Therefore, the two range looks differ in their azimuth FM rates, by virtue of the different center frequencies used. The difference between the azimuth FM rates is

$$K_{a_2} - K_{a_1} = \frac{2B\Delta f}{cR_0} = K_{a_0}\frac{\Delta f}{f_0} \tag{8}$$

where K_{a_0} is the azimuth FM rate for a look centered at f_0 and is given by

$$K_{a_0} = \frac{2Bf_0}{cR_0} = \tfrac{1}{2}(K_{a_1} + K_{a_2}) \tag{9}$$

i.e., it is the average of K_{a_1} and K_{a_2}.

Note that η_c in (4) and (5) may have a small dependence on range frequency, which creates a shift in the envelopes $W(\eta - \eta_c)$ used in (4) and (5). We note, for the ERS-1 parameters to be considered later, the dependence is only in the order of 1 ms [9], and the envelope shift can be ignored. However, the change in η_c with range frequency gives rise to an offset frequency which is not negligible in the MLCC estimate described below, and its compensation is an important part in that class of algorithm.

B. The MLCC Cross-Correlation Algorithm

In the MLCC method, the ACCC angles of the two range looks are computed, and then the difference between these two angles is obtained.

Let us examine first the general case in which a signal $S(\eta)$ with an azimuth FM rate K_a and an envelope centered around η_c is given by

$$S(\eta) = W(\eta - \eta_c)\exp(-j\pi K_a\eta^2). \tag{10}$$

At azimuth time η, the *instantaneous* frequency of the signal is $-K_a\eta$, and the change in phase angle per azimuth sample is $-2\pi K_a\eta\Delta\eta = -2\pi K_a\eta/F_a$, which is the familiar result when $\Delta\eta = 1/F_a$ is the azimuth sample spacing and F_a is the radar PRF. The *average* frequency of the signal is then $-K_a\eta_c$, since the azimuth envelope is symmetrical and centered around η_c, and the *average* CCC angle is $2\pi K_a\eta_c/F_a$. In practice, the summation is taken over a selected azimuth time interval, typically one to two seconds, for each range cell so that the range-dependent ACCC is defined by

$$\overline{C(\eta)} = \sum_{\eta} S(\eta)S^*(\eta + \Delta\eta) \tag{11}$$

where S^* denotes the complex conjugate of S.

Denote the ACCC of Look 1 by $\overline{C_1(\eta)}$ and of Look 2 by $\overline{C_2(\eta)}$. Applying the above analysis, the ACCC angles ϕ_{L_1} and ϕ_{L_2} of Look 1 and Look 2, respectively, are given by

$$\phi_{L_1} = \arg[\overline{C_1(\eta)}] = \frac{2\pi K_{a_1}\eta_c}{F_a} \tag{12}$$

$$\phi_{L_2} = \arg[\overline{C_2(\eta)}] = \frac{2\pi K_{a_2}\eta_c}{F_a}. \tag{13}$$

Then their difference $\Delta\phi$ is

$$\Delta\phi = \phi_{L_2} - \phi_{L_1} = \frac{2\pi(K_{a_2} - K_{a_1})\eta_c}{F_a}. \tag{14}$$

In practice, this is obtained by

$$\Delta\phi = \arg\{\overline{C_1(\eta)}\,[\overline{C_2(\eta)}]^*\}. \tag{15}$$

Using (8) and (9), (14) can be rewritten as

$$\Delta\phi = 2\pi\frac{\Delta f}{f_0}\frac{K_{a_0}\eta_c}{F_a} = -2\pi\frac{\Delta f}{f_0}\frac{f_{\eta_c}}{F_a}. \tag{16}$$

The last step has used the fact the instantaneous frequency at the Doppler centroid is

$$f_{\eta_c} = -K_{a_0}\eta_c. \tag{17}$$

Since $\Delta\phi$ is much less than a radian, angle wrap around is not a problem and the parameter f_{η_c}

$$f_{\eta_c} = -\frac{f_0 F_a \Delta\phi}{2\pi\Delta f} \tag{18}$$

determined from (16) is the *absolute* Doppler centroid frequency.

However, in the presence of noise and multiple targets, the value of f_{η_c} so determined may not be accurate enough. To improve its accuracy, the fractional PRF part f'_{η_c} is determined by a more accurate method, and the f_{η_c} estimate of (18) is used to obtain the Doppler ambiguity M. Then, the estimate of f_{η_c} can be refined as follows:

From (9), (12), and (13), the fractional PRF part is obtained from the average (aliased) phase increment by

$$f'_{\eta_c} = -\frac{F_a}{2\pi}\frac{\phi_{L_1}+\phi_{L_2}}{2}. \tag{19}$$

This method is similar to that proposed by Madsen [4]. Since one or both of the ACCC angles ϕ_{L_i} may have been wrapped around, a simple discontinuity detector is used to set f'_{η_c} to within the interval $\pm F_a/2$. The error tolerance in the two ACCC angles is relatively high; an error of 5° in the ACCC angles causes an error of only $0.014\,F_a$ in f'_{η_c}.

The Doppler ambiguity is then estimated as

$$M = \text{round}\left(\frac{f_{\eta_c} - f'_{\eta_c}}{F_a}\right) \tag{20}$$

and the remainder

$$MF_a - (f_{\eta_c} - f'_{\eta_c}) \tag{21}$$

is mainly a measure of the accuracy of the f_{η_c} estimate of (18). To be conservative, a general rule of thumb is to reject the estimate of f_{η_c} when the magnitude of the remainder exceeds 1/3 of the PRF.

Finally, the ambiguity is used to refine the value of f_{η_c} by

$$f_{\eta_c} = f'_{\eta_c} + MF_a. \tag{22}$$

Basically, the difference between the two ACCC angles gives the Doppler ambiguity, and their sum gives the fractional PRF part. In the implementation, the steps are as follows.

1) Compute the ACCC angles $\phi_{L_1}(\tau)$ and $\phi_{L_2}(\tau)$ per range gate; these two angles vary with range time τ.
2) Compute $f'_{\eta_c}(\tau)$ as a function of range using (19). Then fit a low order polynomial to express the range dependence. Take the discontinuities at $\pm F_a/2$ into account.
3) Compute $\Delta\phi(\tau)$ between the two looks from (10) and take its average over all range gates. The average value of $\Delta\phi$ corresponds to that at midrange.
4) Compute the first estimate of f_{η_c} from (18) and the Doppler ambiguity M from (20) at midrange. Then using the range varying $f'_{\eta_c}(\tau)$ found in step 2, the refined value of $f_{\eta_c}(\tau)$ is computed from (22) as a function of range.

The difference between the MLCC and DLR algorithms lies in the fact that the former operates in the range time domain, and the latter in the range frequency domain. In the DLR algorithm, the slope of the ACCC angle with respect to range frequency is measured. But the frequency domain slope can be corrupted by fluctuations in the ACCC angle due to mixing of targets at widely different ranges (as K_a is a function of range time).

To alleviate this problem and to obtain f_{η_c} as a function of range, range compression is performed first in the DLR algorithm. The range compressed data is then segmented into range time blocks, and the DLR algorithm is applied to each block which involves a range FFT to transform the data back to the range frequency domain. This extra set of FFT's increases the computation requirement, in comparison with the MLCC algorithm. Furthermore, there is still mixing of targets within the block, which may require more averaging. In comparison, the MLCC algorithm processes range compressed data in the range time domain, thus eliminating any mixing of targets in the range direction.

As an example of the computing requirements, which are dominated by FFT's and ACCC's, consider a range line with 4-K samples. Assume a block size of 256 samples in the DLR algorithm and a look length of 1-K samples in the MLCC algorithm. Then the DLR algorithm requires two 4-K FFT's per range line for range compression followed by sixteen 256-point FFT's to transform the data back to the range frequency domain. In comparison, the MLCC algorithm requires only one 4-K FFT and two 1-K FFT's per range line, or about half as much FFT computation as the DLR algorithm. Also, due to the 1-K IFFT length in the MLCC algorithm, the number of ACCC's is 2-K per range line for both looks. This is again half the amount of ACCC's required by the DLR algorithm, which is 4-K per range line. Therefore, the MLCC algorithm requires half the total number of arithmetic operations when compared to the DLR algorithm.

The accuracy of the MLCC method depends upon the range look bandwidth and the look separation. Let W_s be the range bandwidth of the signal. The optimal separation of the looks is found to be $\Delta f = 2W_s/3$ and the optimal look bandwidth is $W_s/3$. The derivations of these properties are given in the Appendix.

The MLCC algorithm does not require the data to be acquired in a continuous mode, as the CCC values are computed on pairs of consecutive azimuth samples. For this reason, it is directly applicable to ScanSAR data which will be acquired in discrete bursts for each subswath beam.

C. The MLBF Beat Frequency Algorithm

The operation of the MLBF algorithm can also be understood by examining what happens to a single point target. Treating each range look as an azimuth time series in one range cell, the MLBF algorithm begins by multiplying the two range looks given in (4) and (5) together (conjugating the second look). Using these equations, the resultant beat signal $S_b(\eta)$ for a point target is given by

$$\begin{aligned} S_b(\eta) &= S_1(\eta)S_2^*(\eta) \\ &= |W(\eta-\eta_c)|^2 \exp\left[j\pi(K_{a_2}-K_{a_1})\,\eta^2\right]. \end{aligned} \tag{23}$$

Because K_{a_2} and K_{a_1} are quite close to one another and the Doppler bandwidth is limited, the signal frequencies expressed by (23) are confined to a narrow bandwidth. Thus a distinct beat frequency is discernible, and from (8), (17), and (23), this average beat frequency f_b is

$$\begin{aligned} f_b &= (K_{a_2}-K_{a_1})\eta_c \\ &= K_{a_0}\frac{\Delta f}{f_0}\eta_c \\ &= -\frac{\Delta f}{f_0} f_{\eta_c}. \end{aligned} \tag{24}$$

The *absolute* Doppler centroid frequency is then estimated by

$$f_{\eta_c} = -\frac{f_0}{\Delta f} f_b. \tag{25}$$

Similar to the MLCC algorithm, the MLBF algorithm also requires averaging to improve its accuracy when dealing with real SAR data. In the implementation, the beat signal and its FFT are computed per range gate. The average power of the FFT's is computed over the entire range swath. Then the peak in the signal spectrum is detected to give the midrange f_{η_c} and the Doppler ambiguity. Finally, similar to the MLCC algorithm, the estimated range-dependent f'_{η_c} will guide the algorithm to refine f_{η_c} as a function of range.

For a very wide range swath and high f_{η_c} slope as a function of range, it may be necessary to segment the swath into range blocks. The Doppler ambiguity at the middle of each block is then determined.

To improve peak detection, the following procedures can be used. The beat signal of a point target is simulated, and its FFT gives the ideal impulse response. Then a normalized correlation between the impulse response and the power of the averaged FFT's is performed (a form of matched filtering in which the result lies between -1 and $+1$). The maximum value of the correlation also gives a "goodness of fit" which proves to be useful in selecting the best results between the MLBF and MLCC algorithms.

When using the MLBF algorithm on ScanSAR data, the data must be zero padded in the data "gaps." If short FFT's are performed directly on the bursts instead, the impulse response will be too broad for an accurate estimation of the peak position of the beat signal spectrum. The zero padding results in modulation artifacts in the spectrum which may affect the accuracy of detecting the peak position (see Section IV-E). One alternative is to apply a power spectrum estimation technique to the beat signal frequency without resorting to transform methods [10]. Another alternative is to only use the MLCC algorithm for ScanSAR data, averaging more data as necessary for high contrast scenes.

D. The Integrated Doppler Centroid Estimation Scheme

An integrated scheme to determine the absolute Doppler centroid frequency is shown in Fig. 1. The Doppler ambiguity is estimated using both the MLBF and MLCC algorithms, and then the best result is selected using a "performance" criterion. The fractional PRF estimate is obtained conveniently as the ACCC angles are already computed in the MLCC algorithm.

The scheme is simpler than it first appears, as the computation is dominated by the extraction of the range looks, which is common to each algorithm. It is best to do range compression during look extraction to keep the range dependencies distinct, and to minimize signal interference in the MLBF algorithm. Since the two DAR algorithms compliment each other in terms of scene contrast, the proposed method can work well by averaging only a limited number of range lines.

The criteria which have been found useful for selecting the best of the MLBF and MLCC results are as follows.

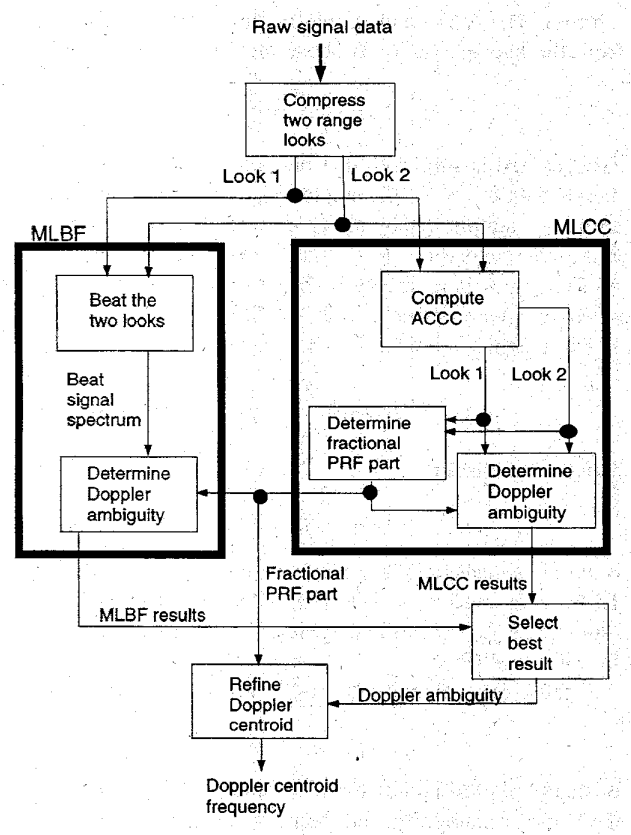

Fig. 1. The integrated doppler centroid estimation scheme.

Normalized Correlation: The "impulse response" of a point target is computed for the MLBF algorithm. The normalized correlation can then be computed between the impulse response and the beat frequency spectrum. If the normalized correlation is above a certain threshold, say 0.6, then accept the MLBF result.

Consistency of Estimate: Segment the data into azimuth blocks. Perform estimates on each block, and compare the consistency of each algorithm.

Scene Contrast: Empirically establish the performance of the MLBF and MLCC algorithms as a function of scene contrast. The DAR algorithm selection is then based upon the measured scene contrast. A measure of scene contrast C_s is suggested by Madsen [4]:

$$C_s = \frac{\langle I \rangle^2}{\langle I^2 \rangle} \tag{26}$$

where I is the image intensity and $\langle . \rangle$ denotes the average value.

III. Multitarget Analysis

In the previous section, we explained the operation of the DAR algorithms by examining the response to a single point target. In order to understand the algorithm's behavior with real SAR data, we will first analyze the simplest multitarget case of two targets, and then generalize to a case with more than two targets. In this way we will show that the MLCC algorithm works best with low contrast scenes and MLBF with

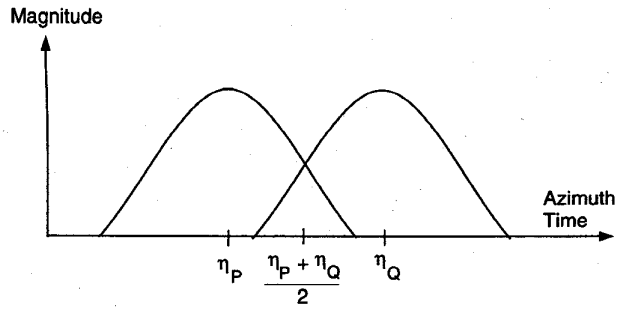

Fig. 2. Overlap of two targets.

high contrast ones, due to the fact that interference between multiple targets affects the two algorithms in different ways.

A. Phase Histories of Two Targets

Consider two targets T_P and T_Q which are in the same range cell and are separated by $\eta_Q - \eta_P$ seconds. If their envelopes overlap, as illustrated in Fig. 2, their phases will interfere with each other and affect the performance of the algorithms.

For the two targets, let the following be in effect.

η	discrete azimuth time with any arbitrarily chosen origin;
$\Delta\eta$	$1/F_a$;
η_P	azimuth time of closest approach for Target T_P;
η_Q	azimuth time of closest approach for Target T_Q;
P	complex amplitude for Target T_P;
Q	complex amplitude for Target T_Q;
$W(\eta)$	azimuth envelope;
$L_1(\eta)$	range compressed signal of Look 1 at range gate of targets;
$L_2(\eta)$	range compressed signal of Look 2 at range gate of targets;
$L_{1_P}(\eta)$	range compressed Target T_P in Look 1;
$L_{1_Q}(\eta)$	range compressed Target T_Q in Look 1;
$L_{2_P}(\eta)$	range compressed Target T_P in Look 2;
$L_{2_Q}(\eta)$	range compressed Target T_Q in Look 2.

Looks 1 and 2 are one-dimensional signals since only the range gate containing the compressed targets is considered.

From (4) and (5), ignoring the irrelevant phase term due to R_0 and some other range terms due to range compression, the range compressed signals are

$$\begin{aligned} L_1(\eta) &= L_{1_P}(\eta) + L_{1_Q}(\eta) \\ &= PW(\eta - \eta_c - \eta_P)\exp\{-j\pi K_{a_1}(\eta - \eta_P)^2\} \\ &\quad + QW(\eta - \eta_c - \eta_Q)\exp\{-j\pi K_{a_1}(\eta - \eta_Q)^2\} \end{aligned} \tag{27}$$

$$\begin{aligned} L_2(\eta) &= L_{2_P}(\eta) + L_{2_Q}(\eta) \\ &= PW(\eta - \eta_c - \eta_P)\exp\{-j\pi K_{a_2}(\eta - \eta_P)^2\} \\ &\quad + QW(\eta - \eta_c - \eta_Q)\exp\{-j\pi K_{a_2}(\eta - \eta_Q)^2\}. \end{aligned} \tag{28}$$

It has been assumed that the target trajectory stays within one range cell during the azimuth exposure; this gives the maximum possible interference duration between the targets within a range gate. Range cell migration effects will be discussed in Section III-B.

Since $W(0)$ is the maximum value of the antenna weighting, the peak for Target T_P occurs at azimuth time $\eta_c + \eta_P$, and Target T_Q at time $\eta_c + \eta_Q$.

B. Effect on the MLCC Algorithm

Consider the two targets T_P and T_Q first. The ACCC between adjacent azimuth samples for Look 1 is defined as

$$\overline{C_1(\eta)} = \sum_{\eta} L_1(\eta) L_1^*(\eta + \Delta\eta). \tag{29}$$

Again, η assumes discrete values and adjacent samples are separated by $\Delta\eta$.

By expanding to show the contribution of each target, we obtain

$$\begin{aligned} \overline{C_1(\eta)} &= \overline{C_{1PP^*}(\eta)} + \overline{C_{1QQ^*}(\eta)} \\ &\quad + \overline{C_{1PQ^*}(\eta)} + \overline{C_{1P^*Q}(\eta)}. \end{aligned} \tag{30}$$

The four terms in (30) are as follows.

- The first term is the ACCC between adjacent azimuth samples due to Target T_P alone, and from (27) we see that

$$\begin{aligned} \overline{C_{1PP^*}(\eta)} &\approx |P|^2 \sum_{\eta} W^2(\eta - \eta_c - \eta_P) \\ &\quad \cdot \exp\{-j\pi K_{a_1}(\eta - \eta_P)^2 \\ &\quad + j\pi K_{a_1}(\eta + \Delta\eta - \eta_P)^2\} \\ &\approx |P|^2 \sum_{\eta'} W^2(\eta' - \eta_c)\exp(j2\pi K_{a_1}\eta'\Delta\eta) \end{aligned} \tag{31}$$

  where η' is a dummy variable replacing $\eta - \eta_P$. The first approximation utilizes the fact that $W(\eta - \eta_c - \eta_P) \approx W(\eta - \eta_c - \eta_P + \Delta\eta)$. The second approximation is due to the fact that the contribution of $K_{a_1}\Delta\eta^2$ to the phase is small enough to be ignored in practice.
- Similarly, the second term is the ACCC due to Target T_Q alone:

$$\begin{aligned} \overline{C_{1QQ^*}(\eta)} &\approx |Q|^2 \sum_{\eta} W^2(\eta - \eta_c - \eta_Q) \\ &\quad \cdot \exp\{-j\pi K_{a_1}(\eta - \eta_Q)^2 \\ &\quad + j\pi K_{a_1}(\eta + \Delta\eta - \eta_Q)^2\} \\ &\approx |P|^2 \sum_{\eta'} W^2(\eta' - \eta_c)\exp(j2\pi K_{a_1}\eta'\Delta\eta) \end{aligned} \tag{32}$$

  where η' is a dummy variable replacing $\eta - \eta_Q$. The angle of $\overline{C_{1QQ^*}(\eta)}$ is the same as that of $\overline{C_{1PP^*}(\eta)}$. The first and second terms $\overline{C_{1PP^*}(\eta)}$ and $\overline{C_{1QQ^*}(\eta)}$ in (30) are the desired ones.

- The third term is the ACCC due to Target T_P and the complex conjugate of Target T_Q:

$$\begin{aligned}\overline{C_{1PQ^*}(\eta)} &= PQ^* \sum_{\eta} W(\eta-\eta_c-\eta_P)W(\eta-\eta_c-\eta_Q)\\ &\quad\cdot \exp\{-j\pi K_{a_1}(\eta-\eta_P)^2\\ &\quad + j\pi K_{a_1}(\eta+\Delta\eta-\eta_Q)^2\}\\ &= PQ^* \sum_{\eta'} W(\eta'-\eta_c+\epsilon)W(\eta'-\eta_c)\\ &\quad\cdot \exp\{j\pi K_{a_1}(2\eta'+\Delta\eta+\epsilon)(\Delta\eta-\epsilon)\} \quad (33)\end{aligned}$$

where η' is a dummy variable replacing $\eta-\eta_Q$ and

$$\epsilon = \eta_Q - \eta_P \quad (34)$$

is the separation between the two targets.

- Similarly, the fourth term is

$$\begin{aligned}\overline{C_{1P^*Q}(\eta)} &= P^*Q \sum_{\eta} W(\eta-\eta_c-\eta_P)W(\eta-\eta_c-\eta_Q)\\ &\quad\cdot \exp\{-j\pi K_{a_1}(\eta-\eta_Q)^2\\ &\quad + j\pi K_{a_1}(\eta+\Delta\eta-\eta_P)^2\}\\ &= P^*Q \sum_{\eta'} W(\eta'-\eta_c+\epsilon)W(\eta'-\eta_c)\\ &\quad\cdot \exp\{j\pi K_{a_1}(2\eta'+\Delta\eta+\epsilon)(\Delta\eta+\epsilon)\} \quad (35)\end{aligned}$$

where η' is again a dummy variable replacing $\eta-\eta_Q$.

Similar results are obtained for Look 2. The algorithm then finds the angle difference between $\overline{C_1(\eta)}$ for Look 1 and $\overline{C_2(\eta)}$ for Look 2.

In the case that the two targets are so far part that the side lobes of one have negligible effects on the other target, then the last two terms in (30) can be ignored leaving only the first two terms $\overline{C_{1PP^*}(\eta)}$ and $\overline{C_{1QQ^*}(\eta)}$. The first term is the ACCC between adjacent azimuth samples due to Target T_P alone and the second term due to Target T_Q alone. Then the angles of $\overline{C_1(\eta)}$, $\overline{C_{1PP^*}(\eta)}$ and $\overline{C_{1QQ^*}(\eta)}$ in (30) are all the same. Similarly, the same result holds for Look 2. Hence, the Doppler centroid frequency obtained for two targets in the MLCC algorithm is that same as the one-target case; that is, the correct Doppler centroid is determined.

In a more general case of two targets, the terms $\overline{C_{1PQ^*}(\eta)}$ and $\overline{C_{1P^*Q}(\eta)}$ can introduce an error in the angle of $\overline{C_1(\eta)}$, and similarly for Look 2. Unfortunately, these two errors for the two looks are not the same, therefore they do not cancel each other in the angle difference.

For multiple targets, the terms $\overline{C_{1PQ^*}(\eta)}$ and $\overline{C_{1P^*Q}(\eta)}$ in (33) and (35) respectively have zero mean. Hence, the presence of multiple targets actually helps to reduce their adverse effects. Statistically, the more the number of targets, the closer will be the angle of $\overline{C_1(\eta)}$ to the case of a point target. The same argument applies to Look 2. Hence, the difference between the two angles $\overline{C_1(\eta)}$ and $\overline{C_2(\eta)}$ improves in accuracy when the number of targets increases. In this way, the MLCC algorithm performs better in scenes of low contrast.

It remains to discuss the effect of range cell migration which has been ignored in the development above. The energy in any one particular target may traverse more than one range cell in the area being averaged in the received signal. Then the Doppler centroid contribution of this target will be biased according to which part of the target is in the range cell being considered. A similar bias will occur when the target is only partially exposed within the azimuth averaging region.

However, many targets are being averaged in practice, and the Doppler frequency biases caused by partial targets will tend to average out to zero bias. In effect this means that the ACCC computed is equivalent to that which would be obtained if the central part of the target is exposed in the current range cell. Furthermore, when obtaining the ACCC angle difference between looks, more averaging is performed in the range direction, helping to remove any bias. For these reasons, range cell migration correction does not have to be performed in the Doppler centroid estimation algorithms under discussion.

C. Effect on the MLBF Algorithm

Again, consider the two targets T_P and T_Q first. From (27) and (28), the beat signal is

$$\begin{aligned}L_b(\eta) &= L_1(\eta)L_2^*(\eta)\\ &= L_{1_P}(\eta)L_{2_P}^*(\eta) + L_{1_Q}(\eta)L_{2_Q}^*(\eta)\\ &\quad + L_{1_P}(\eta)L_{2_Q}^*(\eta) + L_{1_Q}(\eta)L_{2_P}^*(\eta). \quad (36)\end{aligned}$$

The above holds for any two targets in general regardless of their separation. The four terms corresponds to the four different components.

- The first term represents the beat signal generated by Target T_P alone.
- The second term represents the beat signal generated by Target T_Q alone.
- The third and fourth terms are the signals generated by the cross beating between the two targets.

Using (27) and (28) again, (36) can be rewritten as

$$\begin{aligned}L_b(\eta) &= |P|^2W^2(\eta-\eta_c-\eta_P)\\ &\quad\cdot \exp\{-j\pi(K_{a_1}-K_{a_2})(\eta-\eta_P)^2\}\\ &\quad + |Q|^2W^2(\eta-\eta_c-\eta_Q)\\ &\quad\cdot \exp\{-j\pi(K_{a_1}-K_{a_2})(\eta-\eta_Q)^2\}\\ &\quad + PQ^*W(\eta-\eta_c-\eta_P)W(\eta-\eta_c-\eta_Q)\\ &\quad\cdot \exp\{-j\pi K_{a_1}(\eta-\eta_P)^2 + j\pi K_{a_2}(\eta-\eta_Q)^2\}\\ &\quad + P^*QW(\eta-\eta_c-\eta_P)W(\eta-\eta_c-\eta_Q)\\ &\quad\cdot \exp\{j\pi K_{a_2}(\eta-\eta_P)^2 - j\pi K_{a_1}(\eta-\eta_Q)^2\}. \quad (37)\end{aligned}$$

The FFT of $L_b(\eta)$ is equal to the sum of the FFT's of the above 4 terms.

- The FFT of the first term can be considered to be the "impulse response" of a single target using the MLBF algorithm. For target P, this impulse response peaks at the frequency

$$f_P = -(K_{a_1}-K_{a_2})\,\eta_c \quad (38)$$

which follows from the development leading to (24).

- The FFT of the second term also peaks at the same frequency

$$\begin{aligned} f_Q &= f_P \\ &= -\left(K_{a_1} - K_{a_2}\right)\eta_c. \end{aligned} \tag{39}$$

However, there is an additional phase shift in the FFT relative to the FFT of the first term, due to the azimuth time separation $\eta_P - \eta_Q$ between the two targets. This phase term turns out to be very important as it can cause the two targets to interfere destructively.

- The beat frequency of the third term is

$$f_{PQ^*}(\eta) = -K_{a_1}(\eta - \eta_P) + K_{a_2}(\eta - \eta_Q). \tag{40}$$

The FFT of the third term peaks at the frequency equal to the beat frequency at the center of the overlap area shown in Fig. 2. As seen in the figure, the azimuth time of the center is $\eta_c + 0.5(\eta_P + \eta_Q)$. Substituting this for η in (40) and simplifying, we obtain the peak frequency:

$$f_{PQ^*} = -(K_{a_1} - K_{a_2})\,\eta_c - 0.5(K_{a_1} + K_{a_2})\,(\eta_Q - \eta_P). \tag{41}$$

The power at this frequency is less than that for the first or second term, due to the decrease in the antenna weighting in the overlap area and the decrease in the area itself when the target separation increases.

From (38) and (41) we can write

$$f_{PQ^*} = f_P - \Delta f_b \tag{42}$$

where Δf_b is the frequency offset of f_{PQ^*} from f_P:

$$\Delta f_b = 0.5(K_{a_1} + K_{a_2})(\eta_Q - \eta_P). \tag{43}$$

- Similarly, the beat frequency of the fourth term is

$$f_{P^*Q}(\eta) = K_{a_2}(\eta - \eta_P) - K_{a_1}(\eta - \eta_Q). \tag{44}$$

Again, substituting $\eta_c + 0.5(\eta_P + \eta_Q)$ for η into the above and simplifying, we obtain the peak frequency:

$$\begin{aligned} f_{P^*Q} &= -\left(K_{a_1} - K_{a_2}\right)\eta_c + 0.5(K_{a_1} + K_{a_2})\,(\eta_Q - \eta_P) \\ &= f_P + \Delta f_b \end{aligned} \tag{45}$$

which is offset by the same amount from f_P as f_{PQ^*}, with an opposite sign.

To summarize, there are three peak frequency components in the FFT of $L_b(\eta)$, one corresponding to the Doppler centroid, and a "paired-echo" due to the cross beating between the two targets. Fig. 3 shows a typical example of the beat signal spectrum between two targets, when their separation is 0.45 of the 3-dB azimuth beamwidth, and the ideal response is shown as the dashed line. The paired echoes are noted, along with a distortion in the shape of the central beat frequency due to the cross beating.

The MLBF algorithm therefore suffers from the following adverse effects when multiple targets are present. When more than two targets are present in the same range cell, the distortion of the peak beat frequency gets worse, and its power drops in relation to the power in the paired echoes (which now result from the cross beating of all pairs of overlapping targets). As the number of dominant targets increases, the power due to the cross beating can eventually mask out the required beat signal. This explains why the MLBF algorithm does not work so well in low contrast areas, as opposed to areas where a few targets dominate.

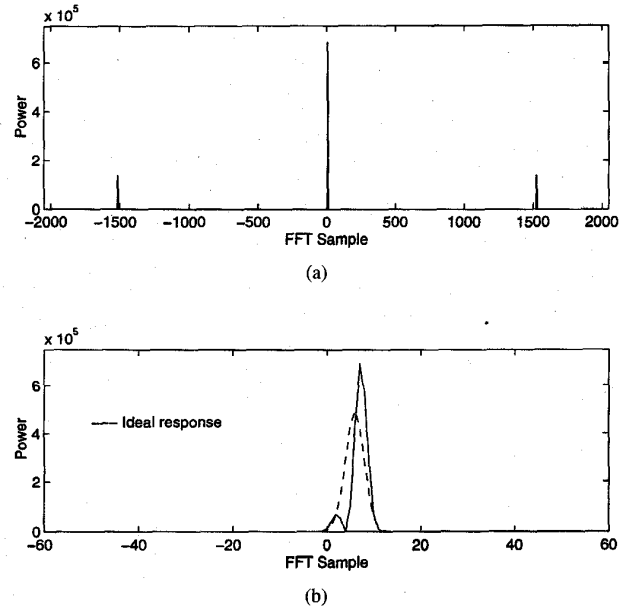

Fig. 3. Spectrum of beat signal of two overlapping targets. (a) Full scale. (b) Expanded scale.

D. Point Target Simulation Experiments

Experiments were performed using simulated point targets and C-band parameters to verify the above analysis. When only two targets are used, and were placed close to each other, the correct ambiguity was detected using the MLBF algorithm, but not using the MLCC algorithm.

Experiments were then performed with a large number of targets distributed at random to simulate radar clutter. The average density of targets in a range cell was varied in 8 steps between a low density of 1/8 targets per azimuth sample to a high density of 1 target per azimuth sample. The following random distributions were assumed: uniform distribution for separation between targets, uniform distribution for target phase, and a Gaussian distribution for target amplitude. In each experiment the input data was generated 50 times, emulating an average more than 50 range cells.

In the MLBF algorithm, the FFT power was summed over the 50 runs, and the sum was normalized to the one-target case. In the MLCC algorithm, the ACCC's of each look were summed over the 50 runs and the angle $\Delta\phi$ calculated between the ACCC's of the two looks. In all the eight cases, the MLCC detected the correct ambiguity, but the MLBF could only do so when the target density is less than or equal to 3/8 targets per PRI. Fig. 4 show the beat signal spectrum of this particular case.

Thus the experiments verify that the MLCC algorithm works best with low contrast scenes, while the MLBF works best with

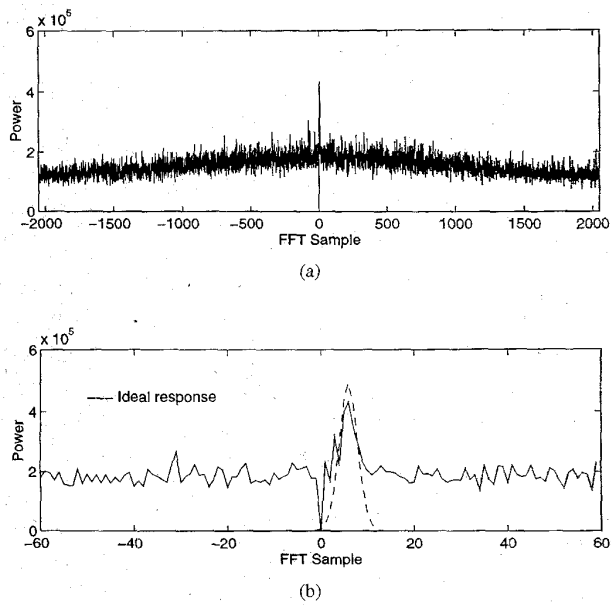

Fig. 4. MLBF response of randomly distributed targets (density of 3/8 targets per azimuth sample). (a) Full scale. (b) Expanded scale.

high contrast scenes, and that one of the two algorithms finds the correct ambiguity with any target density (scene contrast) simulated.

IV. Experiments with Satellite Data

A. Scenes and Parameters

Experiments were performed on the MLBF and MLCC algorithms with real SAR data acquired from ERS-1, the European Space Agency C-band SAR satellite, and JERS-1, the Japanese National Space Agency L-band SAR satellite. Scenes imaged over various terrains were used:

1) Flevoland (farm land, inland sea, two scenes), Holland, ERS-1;
2) Sardegna (mountains, trees), Italy, ERS-1;
3) Island (agriculture, sea, forested mountains, two scenes), Indonesia, ERS-1;
4) Arctic Ocean (two sea ice scenes), Canada, ERS-1;
5) Atlantic Ocean near Newfoundland, Canada, ERS-1;
6) Mt. Fuji (forests and farm land), Japan, JERS-1.

All scenes are acquired from ERS-1, except the Mt. Fuji scene which is acquired from JERS-1. In the case of the ERS-1 scenes, all but one were taken in the yaw-steering mode, where the Doppler ambiguity is normally zero (it was zero in each of the scenes tested). The exception is one of the Flevoland scenes, where the satellite was operated in roll-tilt mode, when the Doppler ambiguity is often away from zero (it was +3 in the scene tested). The JERS-1 scene has a Doppler ambiguity of +1.

A total of 18 different nonoverlapping terrain-diverse areas were selected in the ERS-1 scenes, and 4 in the JERS-1 scene; i.e., a total of 22 areas. Each area contains 4-K range lines by 4-K range pixels, covering an area of approximately 70 km in range by 17 km in azimuth. The parameters of the radar system, and those used in the DAR processing, are shown in Table I. The table contains an entry called *system offset frequency* f_{os} which, similar to the DLR algorithm, is a systematic offset to be subtracted from the measured value of $f_{\eta c}$ in the MLCC algorithm (it is not needed in the MLBF algorithm). This offset frequency depends upon the antenna characteristics, and must be calibrated for each satellite. It was first introduced by Balmer [8] and we have developed a mathematical model [9] to show how it originates from the dependence of antenna pointing angle on transmitted frequency.

TABLE I
ERS-1 and JERS-1 Parameters

Parameters	ERS-1	JERS-1
Centre transmitted frequency, f_0	5.3 GHz	1.275 GHz
Range sampling rate, F_r	18.96 MHz	17.076 MHz
Pulse width, T_r	37.1 μs	35.0 μs
Range FM rate, K_r	0.41888 MHz/μs	0.4286 MHz/μs
PRF, F_a	1679 Hz	1555 Hz
Look separation, Δf	10.8 MHz	10.8 MHz
Look bandwidth, W_l	4 MHz	4 MHz
System offset frequency, f_{os}	1400 Hz	-901 Hz

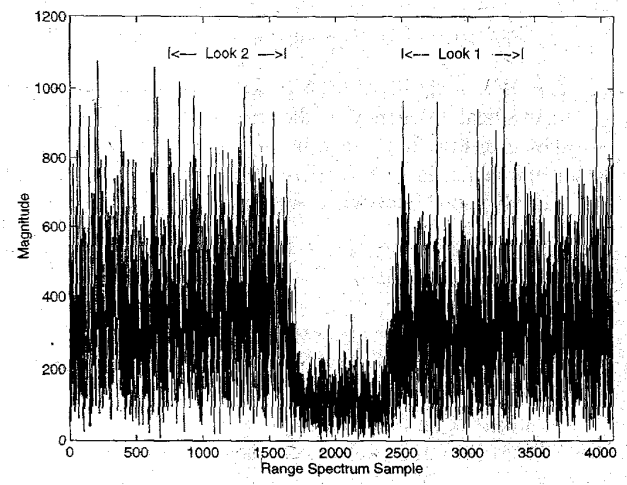

Fig. 5. Location of looks taken from the range spectrum (ERS-1 data, Flevoland roll-tilt scene).

Fig. 5 shows the magnitude of the range spectrum of a typical range line, showing the placements of the looks used in the experiments. The signal bandwidth is about 15 MHz, and a look bandwidth of 4 MHz is selected for the experiments. The ratio of the look bandwidth to signal bandwidth is then about 0.27 which is close to the optimal value derived in the Appendix.

The Doppler centroid frequency of each scene was first obtained by the traditional method of peak search in the Doppler spectrum, with the Doppler ambiguity resolved by the azimuth look correlation method. This Doppler centroid frequency was then used as the measurement reference. Reference [1] cites the achievable accuracy to be about 10 Hz, but practicable experience has shown that this estimate has a standard deviation of about 20 Hz.

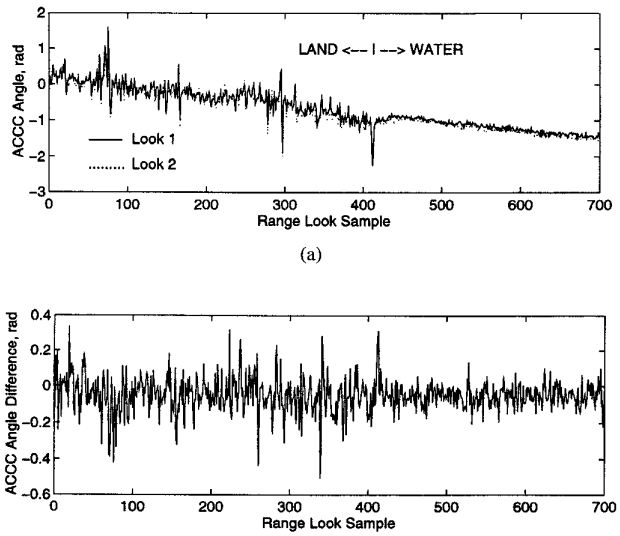

Fig. 6. ACCC angles estimated from the roll-tilt Flevoland scene. (a) ACCC angles of the two looks. (b) ACCC angle difference between the two looks.

B. Experiments with the MLCC Method

Of the 22 areas tested using the MLCC method, 21 gave the correct ambiguity with its remainder given by (21) less than 0.3 PRF. The exception was an area in one of the Island scenes, where the number of range lines averaged had to be increased to 8 K before the correct Doppler ambiguity was obtained.

Given that the correct ambiguity was obtained, the rms difference between the Doppler centroid estimated from the MLCC method and the reference values obtained from the traditional approaches was only 36 Hz. The largest difference was 105 Hz, and the next largest was 69 Hz. Note that the fractional PRF accuracy of the MLCC method (as well as for the MLBF method) depends upon that of the ACCC estimator used in both methods.

Fig. 6 shows typical variations of the ACCC angles for looks 1 and 2, and their difference, as a function of range. The slopes of the ACCC angles are an indication of the range variation of the Doppler centroid. The area averaged covers both land (Flevoland polder) and water (the Zuiderzee), as indicated in the figure. The water area exhibits less ACCC angle fluctuations than the land area, because it has less contrast. Even though the ACCC angle difference is small compared with its standard deviation as shown in Fig. 6(b), it is detectable when averaged over the range swath of 700 output range cells, and the absolute Doppler centroid can be estimated reliably to within 1/3 of the PRF.

C. Experiments with the MLBF Method

MLBF experiments were performed with the same 22 areas used in the MLCC experiments. In each experiment, the normalized correlation of the Doppler spectrum with an ideal impulse response was extracted as a quality measure. For averaging areas of 4 K × 4 K samples, the algorithm works well for the land scenes, marginally for the ocean scene and poorly for the ice scenes, as summarized in Table II.

TABLE II
SUMMARY OF DOPPLER AMBIGUITY ESTIMATION RESULTS

Scenes	Contrast	Areas	MLCC	MLBF
ERS-1 C-band				
Flevoland (Roll-tilt)	High	3	√	√
Flevoland (yaw-strd)	High	1	√	√
Sardegna	Medium	1	√	√
Island 1	Medium	3	× (*)	√
Island 2	Medium	3	√	√
Ocean	Medium/Low	1	√	Marginal
Ice 1	Low	3	√	× (*)
Ice 2	Low	3	√	× (*)
JERS-1 L-band				
Mount Fuji	Low	4	√	√

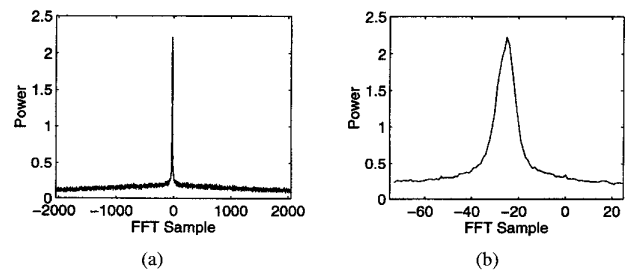

Fig. 7. Beat signal spectrum of roll-tilt Flevoland scene. (a) Full scale. (b) Expanded scale.

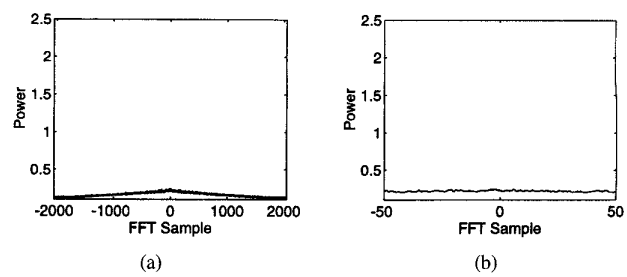

Fig. 8. Beat signal spectrum of ice scene. (a) Full scale. (b) Expanded scale.

Fig. 7 shows a typical averaged spectrum in the land portion of the high-contrast roll-tilt Flevoland scene. A distinctive peak in the vicinity of the desired beat frequency can be easily detected, and the correct Doppler ambiguity can be determined from the peak position. On the other hand, Fig. 8 shows the beat spectrum of a low-contrast ice scene, and the spectrum does not show a similar distinctive peak (which becomes discernible with more averaging as will be discussed later). In this case, the MLBF method just fails to find the correct ambiguity. These two figures show typical spectra for the two extreme cases in contrast.

The normalized correlation coefficient showing the goodness of fit varies between 0.8–0.9 for all land scenes, depending upon the contrast of the scene. The correct ambiguity was detected for these scenes from the spectrum peak, with a remainder less than 0.2 PRF. Experiments were repeated by reducing the averaging region to 1/3 of the range swath, and a

similar high degree of correlation was obtained except when the range gates covered water.

For the ice scenes, the normalized correlation coefficient was found to be about 0.5. When averaging over 1/3 of the range swath, the coefficient fell below 0.5. On the other hand, experiments were also performed to increase the amount of data, by averaging all FFT's over several areas (three areas in each ice scene). In this case, a beat signal spectrum peak was observable and the normalized correlation increased to 0.67. The conclusion is that the algorithm needs to process more data for low contrast scenes, just as MLCC does for high contrast scenes.

In the ocean scene, despite its medium/low contrast, a distinctive peak was still detected with the normalized correlation coefficient found to be 0.7. The correct ambiguity was determined. However, when averaging over only 1/3 of the range swath, the spectrum peak was marginally visible in each group and the normalized correlation coefficient was about 0.5. This suggests that it is best to use full-swath range blocks in the estimation process. It is believed that the performance of MLBF over water depends upon the sea state, and has to be confirmed with more experiments using scenes acquired over water.

D. Summary of Experimental Results

The experiment results for the two DAR algorithms are summarized in Table II. The symbol $\surd$ denotes that the algorithm detects the correct ambiguity, and $\times$ denotes that it does not. For the experiments marked (*), averaging over a larger area than a 4-K $\times$ 4-K block was needed for the respective algorithm to give the correct Doppler ambiguity.

The MLBF algorithm works successfully on high-contrast scenes such as farmland and mountains, but not so well on low contrast ones such as water and ice. A conservative choice of the normalized correlation threshold used to select the MLBF method over the MLCC method was found to be 0.6.

E. ScanSAR Experiments

Further MLBF experiments were performed by using the roll-tilt Flevoland and the yaw-steering Sardegna scenes to simulate a four-beam case of ScanSAR data. Because it correlates only over consecutive azimuth samples, the MLCC algorithm, and its associated fractional PRF estimator, are unaffected by the burst cycles of ScanSAR.

To simulate ScanSAR data, ERS-1 data was segmented into 16 bursts, each of length 64 azimuth samples, and the data gap between adjacent bursts was set to 192 samples (one of the ENVISAT operating modes). The data gaps were filled with zeros before applying the MLBF algorithm. In practice, the interpulse period may not be an integer multiple of the pulse repetition interval; in this case, interpolation has to be performed, or more efficiently, a linear phase adjustment [11] can be made to the data spectrum. However, further study should be performed first to study the adverse effects of using the original data without the interpolation or phase adjustment.

The beat signal spectrum of the Flevoland scene, after zero padding the data gaps, is shown in Fig. 9. The spiky

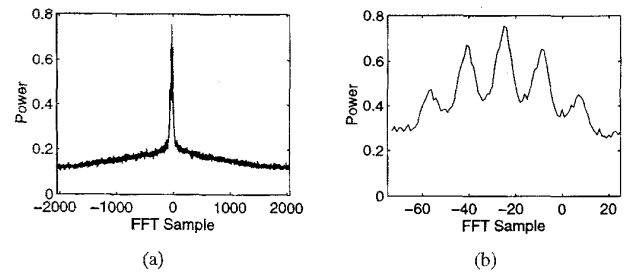

Fig. 9. Beat signal spectrum of simulated ScanSAR data. (a) Full scale. (b) Expanded scale.

appearance, which also appears in the ideal impulse response, is due to the periodic rectangular envelope of the data in the azimuth time domain. The normalized correlation coefficient was found to be 0.8 and the correct ambiguity was obtained. Results of the Sardegna scene were similar, but the normalized correlation was a little lower at 0.7. In both cases, some distortion of the beat spectrum peak was observed. Despite these successful results, more experiments should be performed, as the spectrum peak width is affected by the burst arrangements in the different RADARSAT and ENVISAT ScanSAR beams.

V. Conclusion

An end-to-end scheme to estimate the absolute Doppler centroid frequency has been presented which combines Doppler ambiguity and fractional PRF estimation. The methods are based upon processing two range compressed looks. The scheme includes two complementary algorithms, but the efficiency is high because the algorithms share many of the same preprocessing steps.

The algorithms were tested on blocks of data as small as 4-K $\times$ 4-K, and it was found that the MLBF algorithm works best on high contrast scenes and the MLCC algorithm works best on low contrast ones. Taking advantage of these complementary properties, the proposed scheme incorporates both algorithms, using a quality measure to choose the best estimate. The scheme requires only a reasonable amount of data to operate successfully. Furthermore, the fractional PRF estimator is a by-product of the MLCC DAR.

From the data experiments done so far, we are confident that the new scheme works as well as existing estimators, and likely better because we are able to choose the best result from the two DAR algorithms. When the scheme is implemented in a production processor, more accurate assessments can be made.

The MLCC algorithm is directly applicable to ScanSAR data, while the MLBF algorithm requires zero padding the data gaps. Experiments showed that the performance of the MLBF algorithm on ScanSAR data should be close to the performance on regular beams.

Appendix
Optimal Bandwidth of Range Looks

This appendix derives the optimal bandwidth of the two range looks in the MLCC and MLBF algorithms. As the look bandwidth increases, the measurement information content

increases, but the measurement sensitivity decreases, so an optimal bandwidth must be found.

In the MLCC algorithm, the signal S to be measured is the difference between the averaged CCC angles of the two range looks. In the MLBF algorithm, it can be argued that measuring the peak of the beat signal is equivalent to measuring the CCC angle in the beat signal itself. Regardless of the algorithm, S is then proportional to the look separation Δf, i.e.,

$$S \propto \Delta f. \tag{46}$$

The following development applies to both algorithms.

Assuming measurement noise to be uncorrelated, its variance in the measurement varies inversely as the number of independent range samples available in each look and this number is in turn proportional to the look bandwidth W_{lk}. The noise standard deviation σ_N can then be written as

$$\sigma_N \propto \frac{1}{\sqrt{W_{lk}}}. \tag{47}$$

Let W_s be the available signal bandwidth. The two looks should be placed at the edges of this bandwidth in order to maximize the look separation, thereby increasing the measurement sensitivity. Then we have

$$W_s = W_{lk} + \Delta f. \tag{48}$$

It can be shown that the maximum signal to noise ratio (S/σ_N) occurs when

$$W_{lk} = \tfrac{1}{3} W_s. \tag{49}$$

The corresponding value of look separation Δf is

$$\Delta f = \tfrac{2}{3} W_s. \tag{50}$$

It is recommended to choose a look bandwidth in the range

$$0.25 < W_{lk} < 0.4. \tag{51}$$

For this choice, the signal to noise ratio is within 95% of its maximum value.

Acknowledgment

The authors respectfully acknowledge the contribution of R. Deane of MacDonald Dettwiler for initially introducing the idea of the MLBF algorithm, and the contributions of the reviewers whose ideas have enhanced the paper. The authors would like to thank the European Space Agency and the Canada Center for Remote Sensing for making ERS-1 and JERS-1 data available for the research.

References

[1] F.-K. Li, D. N. Held, J. Curlander, and C. Wu, "Doppler parameter estimation for spaceborne synthetic-aperture radars," *IEEE Trans. Geosci. Remote Sensing,* vol. GRS-23, no. 1, pp. 47–56, Jan. 1985.

[2] I. G. Cumming and J. R. Bennett, "Digital processing of SEASAT SAR data," in *Record IEEE 1979 Int. Conf. Acoustics, Speech and Signal Processing,* Washington, DC, Apr. 2–4, 1979.

[3] A. P. Luscombe, "Taking a broader view: Radarsat adds ScanSAR to its operations," in *Proc. IEEE IGARSS'88 Symp.,* Edinburgh, Scotland, 1988, pp. 1639–1643.

[4] S. N. Madsen, "Estimating the doppler centroid of SAR data," *IEEE Trans. Aerosp. Electron. Syst.,* vol. 25, no. 2, pp. 134–140, Mar. 1989.

[5] K. Kristoffersen, "Time-domain estimation on the center frequency and spread of doppler spectra in diagnostic ultrasound," *IEEE Trans. Ultrason., Ferroelect. Freq. Contr.,* vol. 35, no. 6, pp. 685–700, Nov. 1988.

[6] D. S. Zrnic, "Estimation of spectral moments for weather echoes," *IEEE Trans. Geosci. Electron.,* vol. GE-17, no. 4, pp. 113–128, Oct. 1979.

[7] I. G. Cumming, P. F. Kavanagh, and M. R. Ito, "Resolving the doppler ambiguity for spaceborne synthetic aperture radar," *Remote Sensing: Today's Solutions for Tomorrow's Information Needs,* in *Proc. IEEE IGARSS'86 Symp.,* Zürich, Switzerland, Sept. 8–11, 1986, pp. 1639–1643.

[8] R. Bamler and H. Runge, "PRF ambiguity resolving by wavelength diversity," *IEEE Trans. Geosci. Remote Sensing,* vol. 29, no. 6, pp. 997–1003, Nov. 1991.

[9] I. G. Cumming and F. H. Wong, "Estimating antenna bore-sight angle dependence on radar frequency using SAR doppler centroid estimators," *IEEE Trans. Antennas Propagat.,* to be published.

[10] H. L. Hirsch, *Statistical Signal Characterization.* Norwood, MA: Artech House, 1991.

[11] R. Bamler and M. Eineder, "ScanSAR processing using standard high precision SAR algorithms," *IEEE Trans. Geosci. Remote Sensing,* vol. 34, pp. 212–218, Jan. 1996.

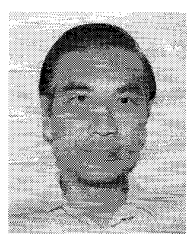

Frank Wong (M'78) received the B.A.Sc. degree in electrical engineering from McGill University, Canada, in 1969 and the M.A.Sc. degree in electrical engineering from Queen's University, Canada, in 1971. While at MacDonald Dettwiler, he obtained the Ph.D. degree in computer science from the University of British Columbia (UBC), Canada, in 1984, specializing in image processing.

He was with the Computering Devices Company, Ottawa, Canada, as a Signal Processing Engineer. In 1977, he joined MacDonald Dettwiler, where he has been doing research work in SAR processing algorithms. Currently, he is a Senior Research Engineer at MacDonald Dettwiler, and also a Sessional Lecturer at UBC, teaching a course in remote sensing. To perform the research reported here, he spent a six-month term at UBC as a Visiting Industrial Scientist, sponsored by MDA and the BC Advanced Systems Institute.

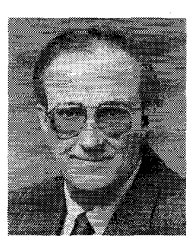

Ian G. Cumming (S'63–M'66) received the B.Sc. degree in engineering physics from the University of Toronto, Canada, in 1961, and the Ph.D. degree in computing and automation from Imperial College, University of London, U.K., in 1968.

Following work in steel mill automation and sonar signal processing algorithms, he has worked on systems for processing perimetric and interferometric radar data, and for the compression of radar data. In 1993, he joined the Department of Electrical Engineering, University of British Columbia, where he holds the MacDonald Dettwiler/NSERC Industrial Research Chair in Radar Remote Sensing. The laboratory supports a research staff of ten engineers and students, working in the fields of squinted SAR processing, satellite two-pass interferometry, airborne perimetric radar calibration requirements, SAR autofocusing, and Doppler estimation.